Enhanced Nucleation of Atomic Layer Deposited Contacts Improves Operational Stability of Perovskite Solar Cells in Air

*James A. Raiford, Caleb C. Boyd, Axel F. Palmstrom, Eli J. Wolf, Benjamin A. Fearon, Joseph J. Berry, Michael D. McGehee, Stacey F. Bent**

J. A. Raiford, Prof. S. F. Bent
Department of Chemical Engineering, Stanford University, Stanford, CA 94305, USA
Email: sbent@stanford.edu

C. C. Boyd
Department of Materials Science and Engineering, Stanford University, Stanford, CA 94305, USA

C. C. Boyd, Dr. A. F. Palmstrom, E. J. Wolf, Dr. J. J. Berry, Prof. M. D. McGehee
National Renewable Energy Laboratory, Golden, Colorado 80401, USA

E. J. Wolf, B. A. Fearon
Department of Applied Physics, Stanford University, Stanford, CA 94305, USA

Prof. M. D. McGehee
Department of Chemical and Biological Engineering, University of Colorado, Boulder, CO 80309, USA

Keywords: atomic layer deposition, perovskite solar cell, barrier layer, nucleation, stability testing

Abstract

Metal-halide perovskites show promise as highly efficient solar cells, light-emitting diodes, and other optoelectronic devices. Ensuring long-term stability is now a major priority. In this study, an ultra-thin (2 nm) layer of polyethylenimine ethoxylated (PEIE) is used to functionalize the surface of C_{60} for the subsequent deposition of ALD SnO_2, a commonly used electron contact bilayer for p-i-n devices. The enhanced nucleation results in a more continuous initial ALD SnO_2 layer that exhibits superior barrier properties, protecting $Cs_{0.25}FA_{0.75}Pb(Br_{0.20}I_{0.80})_3$ films upon direct exposure to high temperatures (200°C) and water. This surface modification with PEIE translates to more stable solar cells under aggressive testing conditions in air at 60°C under illumination. This type of 'built-in' barrier layer mitigates

degradation pathways not addressed by external encapsulation, such as internal halide or metal diffusion, while maintaining high device efficiency up to 18.5%. This nucleation strategy is also extended to ALD VO_x films, demonstrating its potential to be broadly applied to other metal oxide contacts and device architectures.

Introduction

Significant strides have been made over the past several years to understand and address instabilities in metal halide perovskite solar cells induced by external stressors such as moisture, heat, oxygen, or light.[1–4] Researchers have developed more robust perovskite absorbers through compositional tuning,[5–10] modified or replaced unstable contacts,[11–18] introduced additional passivation and barrier layers,[15,19–23] and implemented encapsulation techniques.[24,25] One fabrication technique that has emerged as an effective tool for implementing these strategies is atomic layer deposition (ALD). ALD has been used extensively for carrier-selective contacts and passivation layers in perovskite solar cells due to the precise control it affords over film thickness and composition, as well as the excellent barrier properties of the resulting films.[26,27] In particular, ALD layers have played a critical role in the development of top-performing perovskite-perovskite,[28–30] perovskite-Si,[31–35] and perovskite-CIGS[36] tandem solar cells as both recombination and protective buffer layers.

In many of these cases, an ALD metal oxide is grown on an organic transport layer within the device stack. For example, for perovskite solar cells in the p-i-n architecture, ALD SnO_2 is frequently deposited on a fullerene layer on top of the perovskite as a buffer for the subsequent sputtering of a transparent conducting oxide.[29–36] The physical properties of an ALD film grown on an organic substrate are often different from that grown on an inorganic substrate.

These differences arise from precursor diffusion and subsurface growth, as well as substrate-precursor chemical interactions. As a result, it is important to consider several factors when depositing ALD films on organics, including: 1) the structure and surface functionalization of the organic material, 2) the size and ligand structure of the ALD precursor, 3) the ALD co-reactant, and 4) the deposition temperature.[37–39] Previous studies of ALD nucleation on organic materials have focused primarily on the deposition of aluminum oxide using trimethylaluminum and water.[40,41] One common observation is that subsurface growth occurs on organics with a low density of functional units (e.g. hydroxyls, amines) capable of nucleating ALD and on polymers with functional units located in the backbone chain.[42,43] On the other hand, ALD on highly-branched polymers with a high density of functional units in pendant groups leads to an abrupt polymer/oxide interface.[44,45] In the context of ALD on perovskites, the latter case is desirable to achieve a dense, uniformly deposited film with enhanced barrier properties and more consistent, controllable electronic properties.

Polyethylenimine (PEI) is a polymer with repeating -CH_2CH_2NH- units. The branched version of PEI contains primary, secondary, and tertiary amines and can be ethoxylated (PEIE) to convert a majority (~80%) of the primary amines to hydroxyl groups. This high density of hydroxyl functional groups can act as nucleation sites for ligand exchange reaction with ALD metal-organic precursors. PEI and PEIE have been used effectively in organic photovoltaics and electronics,[46–48] as well as perovskite solar cells,[49,50] as an interfacial layer to modify the work function of adjacent electrodes. Zhou et al. showed that both an intrinsic molecular dipole from amine groups in the polymer physisorbed to the substrate and an interfacial dipole induced by electron transfer from PEIE to the electrode surface contribute to a change in electrode work

function.[51] More recently, PEIE has been used as a nucleation layer for ALD-grown aluminum zinc oxide recombination layers in all-perovskite tandem solar cells.[28]

In this work, we use thin PEIE layers to successfully enhance the nucleation of metal oxides grown by ALD as selective contacts. We show that improved nucleation results in more stable solar cells under aggressive testing conditions in ambient air with simultaneous stressors of heat and illumination. In particular, we study the low-temperature (90°C) growth of ALD SnO_2 from tetrakis(dimethylamino)tin(IV) and water on C_{60} as the electron contacts in p-i-n devices. We first use Auger electron spectroscopy (AES) mapping to quantify the extent to which PEIE improves SnO_2 nucleation on C_{60}. Severe stress tests, such as prolonged exposure to 200°C in air or direct contact with liquid water, of perovskite films capped with PEIE/SnO_2 manifest how an enhancement in nucleation leads to improved barrier properties of ALD films. Finally, we integrate C_{60}/PEIE/SnO_2 contacts into single-junction solar cells with metal rear electrodes. These devices exhibit high initial efficiencies of 18.5% and show a 40% improvement in stability over devices with C_{60}/SnO_2 contacts following continuous operation at 60°C unencapsulated in air for 250 hours. These results demonstrate the importance of improved barrier layers for metal-halide perovskite device stability and outline a future research direction of enhancing nucleation and growth of ALD oxides for functional barrier layers in perovskite optoelectronic devices.

Results and Discussion

While C_{60} and its derivatives (e.g. [6,6]- phenyl-C_{61}-butyric acid methyl ester (PCBM)) have proven to be effective electron contacts in perovskite solar cells,[52–54] they are poor surfaces for the deposition of ALD metal oxides, which rely on the chemisorption of precursors

at the surface to grow. AES elemental maps and line scans of Sn, C and Si for silicon/C_{60} and silicon/PCBM patterned substrates following 10 cycles of ALD SnO_2 (Figure S1 and S2, respectively) show that SnO_2 nucleates and grows much more effectively on Si than either C_{60} or PCBM. Due to hydroxyl termination of its native oxide, the silicon substrate is expected to effectively nucleate SnO_2 growth. If we designate the average Sn signal over the silicon and fullerene surfaces as measured by AES to be σ_1 and σ_2, respectively, then we can define a growth ratio σ_1: σ_2 as a metric for the difference in ALD nucleation between the two surfaces. This growth metric will be dependent upon the characterization technique and number of ALD cycles that are employed. However, given the surface-sensitive nature of AES, the use of only 10 cycles of ALD SnO_2, and the fact that both the organic and Si substrates are present in the same AES scan, we believe this ratio is an appropriate metric to compare nucleation of the metal oxide at each surface.

For the case shown in Figure S1, the ratio of ALD SnO_2 growth on silicon versus C_{60} after 10 cycles is approximately 3:1 (5.3:1 for PCBM shown in Figure S2), indicating significantly less SnO_2 on the C_{60} surface. It would be beneficial to improve upon this poor nucleation for the following reasons. Improving ALD nucleation at the C_{60} surface may promote more rapid formation of a continuous SnO_2 layer in the first few ALD cycles, providing a barrier to precursor diffusion into the C_{60} layer in subsequent cycles and preventing precursor molecules from interacting with the underlying perovskite layer. Better nucleation could also minimize the number of ALD cycles needed to achieve a desired SnO_2 film thickness. Several studies have reported that excessive exposure to metal-organic ALD precursors can damage the perovskite material by etching away organic cations from the perovskite surface.[55–58]

We used the same analysis to investigate the nucleation of ALD SnO_2 on C_{60} that has been coated with a thin layer of PEIE. The thickness of the PEIE layer is approximately 2 nm as measured by spectroscopic ellipsometry and can be controlled by varying the concentration of the PEIE solution (Figure S3). A patterned substrate was prepared with C_{60} on one side and C_{60}/PEIE on the other, and the entire sample was exposed to 10 cycles of ALD SnO_2. The AES elemental map of Sn and average line scans of Sn and C are shown in **Figure 1**. In this case, the ratio of SnO_2 growth on C_{60}/PEIE versus C_{60} is roughly 4.3:1. The PEIE interlayer clearly results in a higher initial coverage of ALD SnO_2 on the surface of the organic. We repeated this AES experiment with ALD vanadium oxide (VO_x), which has recently been used as a hole contact in both n-i-p and p-i-n devices.[59,60] The VO_x was grown at 80°C using vanadium(V) oxytriisopropoxide and water as the metal-organic precursor and co-reactant, respectively. Interestingly, the VO_x also showed more selective growth on C_{60}/PEIE versus C_{60} with a growth ratio of 2.4:1 (Figure S6), indicating that this nucleation strategy is transferrable to other ALD metal oxide contacts that may be relevant to other device architectures.

Atomic force microscopy (AFM) measurements also support the idea that PEIE enhances the nucleation of ALD SnO_2. Topological scans of 3 nm of ALD SnO_2 on C_{60} substrates with and without PEIE are shown in Figure S7. With the addition of PEIE, the SnO_2 grain size is smaller than that of SnO_2 grown on bare C_{60}. The smaller grains indicate that PEIE introduces significantly more nucleation sites for the ALD precursors to react with on the surface. We also used X-ray photoelectron spectroscopy (XPS) depth profiling with a gentle Ar^+ sputter to probe the C_{60}/SnO_2 interface with and without PEIE (Figure S8). High resolution spectra of the Sn3d and C1s peaks were taken between 30 second sputter intervals and were used to calculate relative atomic concentrations of tin and carbon. A qualitative comparison of the two depth profiles

reveals it takes longer to sputter through 50 cycles of ALD SnO_2 with the PEIE nucleation layer than without it, suggesting a more compact ALD barrier layer with the PEIE.

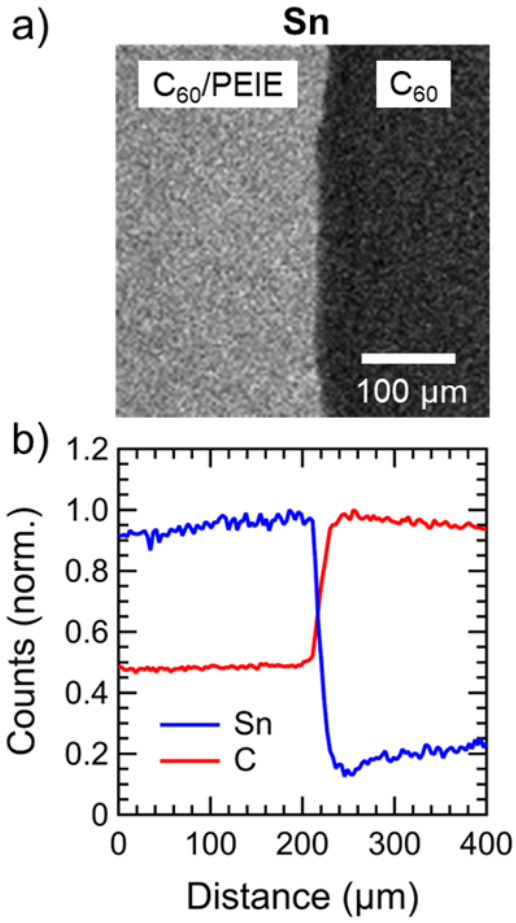

Figure 1: (a) Tin elemental map by Auger electron spectroscopy (AES) of a patterned C_{60} substrate following 10 cycles of SnO_2 ALD. The left side of the C_{60} substrate was coated with a PEIE nucleation layer (from 0.025wt% solution) prior to ALD. The brighter pixels correspond to regions with higher Sn content. (b) Average horizontal line scans of elemental tin and carbon extracted from AES maps.

To evaluate the extent to which better nucleation translates to improved barrier properties of the ALD film, we annealed $Cs_{0.25}FA_{0.75}Pb(Br_{0.20}I_{0.80})_3/C_{60}/SnO_2$ samples on glass with and without a PEIE nucleation layer at 200°C in air. We used 50 cycles of ALD SnO_2 (8 nm on a silicon substrate) for these samples because we have previously shown that this number of cycles

is optimal for SnO_2 contact layers in devices.[31,56] **Figure 2**a shows time lapse images of the films over the course of 120 minutes. The sample without PEIE quickly shows visible yellow bleaching after 15 min, indicating perovskite degradation and the formation of $PbI_{2-x}Br_x$. This degradation continues to propagate throughout the film during the entire duration of the test. In Figure 2b, we also observe a continuous decrease in the perovskite absorbance over time; after 120 minutes the absorbance at 700 nm drops to 36% of its initial value. When PEIE is used to nucleate the ALD SnO_2 layer, the sample shows no signs of visible degradation after 120 minutes. Additionally, the absorbance at 700 nm remains approximately constant with its initial value (Figure 2c). We also exposed the same two types of samples to a drop of water directly on the ALD SnO_2 surface and captured time lapse images of the samples over the course of 10 minutes (Figure 2d). Once again, the sample without PEIE exhibited poor stability, as the water immediately penetrated through the ALD SnO_2 and dissolved the perovskite layer. The SnO_2 layer grown on PEIE was impermeable to the water over the course of the 10 minutes and no degradation of the perovskite was observed. The external stressors applied to the perovskite films during these two tests are quite severe compared to conditions the perovskite is expected to endure throughout subsequent fabrication, encapsulation or operation. Thus, these tests highlight the impact that a high-quality contact/barrier layer can have on protecting the perovskite from various degradation pathways, including thermal-induced decomposition and moisture ingress.

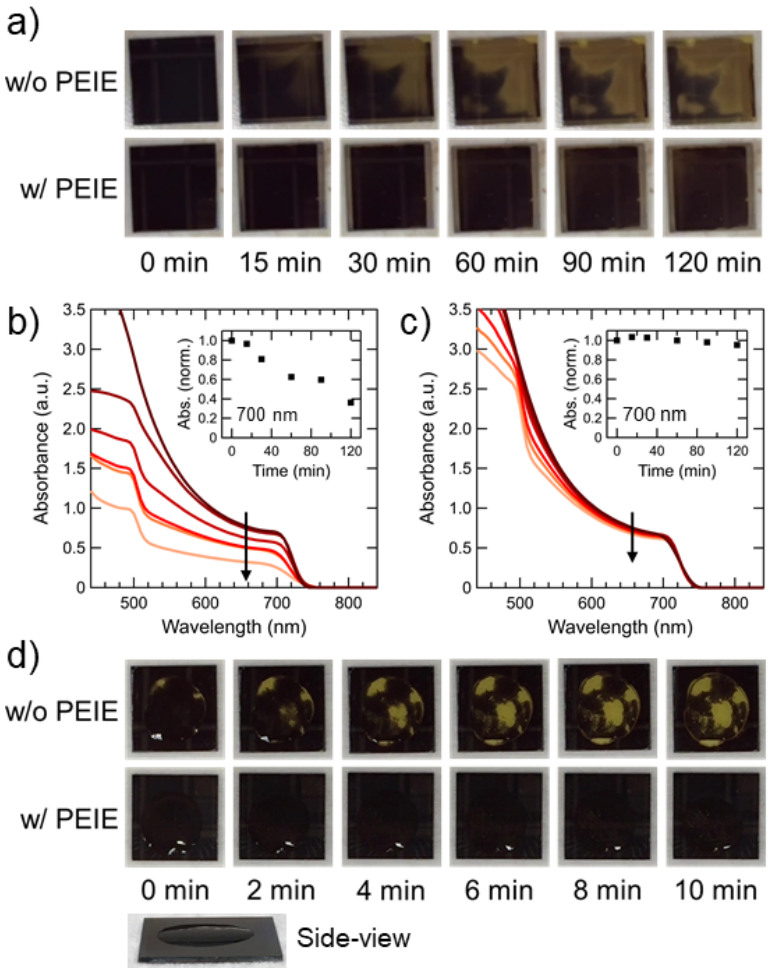

Figure 2: (a) Time lapse images of $Cs_{0.25}FA_{0.75}Pb(Br_{0.20}I_{0.80})_3/C_{60}$ films coated with 50 cycles of ALD SnO_2 with and without a PEIE nucleation layer held at 200°C in air for 120 minutes. Absorbance spectra of the $Cs_{0.25}FA_{0.75}Pb(Br_{0.20}I_{0.80})_3/C_{60}/SnO_2$ films (b) without PEIE and (c) with PEIE over the course of the 120 minute thermal stress test. The arrows indicate the evolution of the absorbance spectra with increasing time. The inset plots show normalized absorbance at 700 nm over time. (d) Time lapse images of identical samples to those in (a) exposed to a drop of water on the SnO_2 surface for 10 minutes. A side-view of the water droplet on the surface is included.

We fabricated p-i-n perovskite solar cells to test the functionality of the improved PEIE/SnO_2 barrier layer in devices with architectures that are very similar to recently reported high performance all-perovskite and perovskite-silicon tandem devices (**Figure 3**a,b).[28,29,31–35] Briefly, we spun 1.68eV-bandgap $Cs_{0.25}FA_{0.75}Pb(Br_{0.20}I_{0.80})_3$ perovskite films onto ITO/glass substrates coated with poly-TPD films as a hole transport layer. We then thermally evaporated 1

nm of LiF, followed by 30 nm of C_{60} as an electron transport layer. Lithium fluoride has been shown to improve voltages in p-i-n perovskite solar cells.[61,62] An ultra-thin layer (2 nm) of PEIE was spun onto the C_{60} using a solution of PEIE in IPA, and SnO_2/ZTO bilayers were deposited using atomic layer deposition as described in detail in previous reports.[32,56] Finally, devices were completed with Au electrodes using thermal evaporation. Further details of device fabrication can be found in the experimental section.

Opaque, wide-bandgap devices with LiF/C_{60}/SnO_2/ZTO/Au top contacts achieved efficiencies above 18%, similar to that of recently reported opaque cells with LiF/C_{60}/BCP/Ag or Au contacts as shown in Figure S9.[28,31] We made cells using PEIE layers from solutions in IPA with both 0.025wt% and 0.05wt% PEIE. The 0.05wt% PEIE interlayer resulted in decreased fill factors, indicating an increase in series resistance, as shown in **Table 1** and Figure S9. However, using a 0.025wt% PEIE in IPA solution (approximately 2 nm PEIE layer measured by spectroscopic ellipsometry), opaque devices with LiF/C_{60}/PEIE/SnO_2/ZTO/Au top contacts achieved efficiencies above 18.5% as shown in Figure 3c, slightly better than their counterparts with LiF/C_{60}/SnO_2/ZTO/Au contacts (Table 1). We also investigated the effects of using a thinner ALD SnO_2 layer with the PEIE on device performance and stability. Figure S10 shows that average device efficiency slightly decreases when the number of ALD SnO_2 cycles is decreased from 50 to 25 cycles, mainly due to a decrease in fill factor and V_{OC} suggesting more leakage current in devices with thinner SnO_2. We note that devices with 50 or 25 cycles of ALD with and without PEIE all have very similar efficiencies. In addition, we repeated the water barrier test from Figure 2d with the thinner SnO_2 layer, and the time lapse images are shown in Figure S11. While the overall impermeability of the thinner 25 cycle ALD SnO_2 on PEIE is better than that of 50 cycles of SnO_2 with no PEIE, it falls short of the water stability

demonstrated by the thicker, PEIE + 50 cycle ALD SnO_2 layer. After 2 minutes, small pinholes became visible as water seeped through and degraded the underlying perovskite. Degradation continued to propagate from these localized weak points compromising the efficacy of the barrier layer. Based on these results, we proceeded with an 8 nm, 50 cycle ALD SnO_2 layer for device stability studies. External quantum efficiency measurements were used to verify current outputs of the devices, as shown in Figure S12. These devices showed very little hysteresis and sustained maximum power outputs close to their reverse scan efficiencies as shown in the inset of Figure 3c.

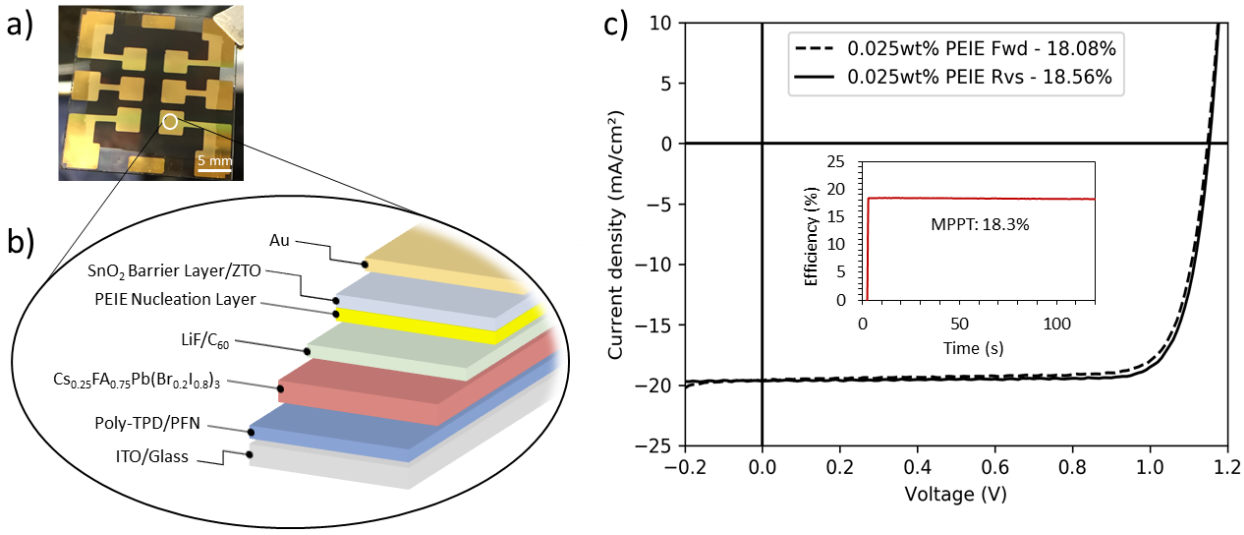

Figure 3: (a) Photograph and (b) schematic of the opaque $Cs_{0.25}FA_{0.75}Pb(Br_{0.20}I_{0.80})_3$ perovskite device structure incorporating a PEIE-nucleated ALD SnO_2 barrier layer. (c) Forward and reverse current-voltage scans and maximum power-point tracking data of the champion device with an improved SnO_2 barrier layer using a 0.025wt% PEIE in IPA nucleation layer.

Table 1: Average JV parameters with standard deviations of cells with and without PEIE nucleation layers.

Device	# Cells	V_{OC} [mV]	J_{SC} [mA/cm^2]	FF [%]	Efficiency [%]
0.025wt% PEIE	45	1129 ± 23	19.71 ± 0.28	79.0 ± 1.2	17.57 ± 0.53
0.05wt% PEIE	27	1110 ± 23	19.72 ± 0.31	76.6 ± 3.3	16.79 ± 0.98
No PEIE	48	1120 ± 29	19.66 ± 0.32	79.6 ± 5.4	17.52 ± 1.28
Champion 0.025wt% PEIE		1154	19.66	81.8	18.56
Champion No PEIE		1162	19.62	80.8	18.43

To further evaluate the barrier layer properties of the ultra-thin PEIE/SnO_2 layer, we placed the highest-performing, unencapsulated opaque cells in a custom-built maximum power tracking setup in ambient air with a relative humidity between 25-30% under ~0.77 sun illumination (lamp spectrum shown in Figure S13) with no active cooling or air flow. The steady state temperature inside the chamber was about 60^{o}C. These combined stresses of elevated temperature, light, and moisture/oxygen exposure were used to evaluate the barrier properties of the ALD layer to halide egress, moisture/oxygen ingress, and metal-halide reactions, all of which have been shown to be primary degradation pathways for perovskite solar cells.[1] We note that these tests are more harsh than standardized protocols for testing the stability of thin-film solar cells,[63] and that all of the stability data reported here was captured without any further encapsulation or protection beyond the PEIE/SnO_2 electron transport layers. In accordance with upcoming protocols from the International Summit on Organic and Hybrid Photovoltaics Stability (ISOS), we have included a supplemental data collection sheet outlining the processing conditions, initial measurements, and aging conditions used in this study. We used Au instead of Ag contacts because Ag has been shown to react more aggressively with the perovskite, although we note that Au has also been shown to react with perovskite degradation products and even

diffuse into the perovskite active layer under similar conditions as the ones used in this study.[22,64,65]

One cell on each substrate was held at its maximum power output using a custom-built tracking system, while the 5 remaining cells on each substrate were held at open circuit for the duration of the test. We aged 8 devices tracked at maximum power and 50 devices held at open circuit, half with 0.025wt% PEIE as a nucleation layer for the SnO_2 and half without PEIE. As shown in **Figure 4** and Figure S14 (champion devices at maximum power), devices without any SnO_2 ALD layer (i.e. only C_{60}/BCP/Ag) degraded in less than 25 hours, and the perovskite turned visibly yellow directly under the metal electrode. In comparison, devices with SnO_2 deposited on the C_{60} were much more stable (despite a brief burn-in period that we attribute to temperature equilibration to 60ºC), with an average of ~60% of their initial efficiency remaining after 250 hours at maximum power as shown in **Table 2** and Figure S15 (average traces of devices held at maximum power). Devices with the PEIE-enhanced ALD SnO_2 barrier layer displayed even better resistance to degradation, maintaining an average of 81.5% of their initial efficiency with the best device maintaining >90% of its initial efficiency, even after 250 hours of operation in ambient air under full illumination and at 60ºC. The time required for these unencapsulated devices to degrade to 80% of their initial power was >1000x longer than that of devices with only organic C_{60}/BCP electron transport layers, as shown in Figure 4. Interestingly, we also found that devices held at V_{OC} degraded more quickly than devices held at their maximum power point, presumably due to acceleration of photochemical reactions with increased voltage and carrier densities within the perovskite layer (Table 2).[66,67] Cells with PEIE-enhanced ALD SnO_2 maintained on average 60.4% of their initial power following 250 hours at V_{OC}, demonstrating a 3x improvement in stability over cells with ALD SnO_2 directly on

C_{60}. Further work is being done to investigate the mechanism behind this acceleration of degradation under open circuit conditions.

Because an excellent barrier layer for perovskite solar cells must prevent reactions between the perovskite active layer and metal contacts, we also aged twelve unencapsulated cells (glass/ITO/poly-TPD/PFN/ $Cs_{0.25}FA_{0.75}Pb(Br_{0.20}I_{0.80})_3$ perovskite/LiF/C_{60}/PEIE or No PEIE/SnO_2/ZTO/Ag) on a hotplate at 85°C in nitrogen in the dark, a simple test that screens whether an encapsulated device will be able to pass the IEC-standard damp heat test.[22,63] We specifically aged cells with silver top contacts, because silver reacts more aggressively with volatile halide species than gold or copper. Over the course of ~670 hours, the cells with the PEIE nucleation layer exhibited minimal loss in power conversion efficiency, with the best device retaining 94% of its initial efficiency (Figure 4b, Figure S16). On the contrary, cells without a PEIE nucleation layer lost all power conversion efficiency (Figure 4b, Figure S16), due to severe metal-halide reactions that corroded the top contacts (Figure 4c). X-ray diffraction of the aged devices showed a negligible amount of crystalline silver remaining at the contacts of the devices without PEIE, whereas the devices with PEIE showed an order of magnitude improvement in their barrier properties as quantified by the amount of silver remaining unreacted after the test (Figure S17).

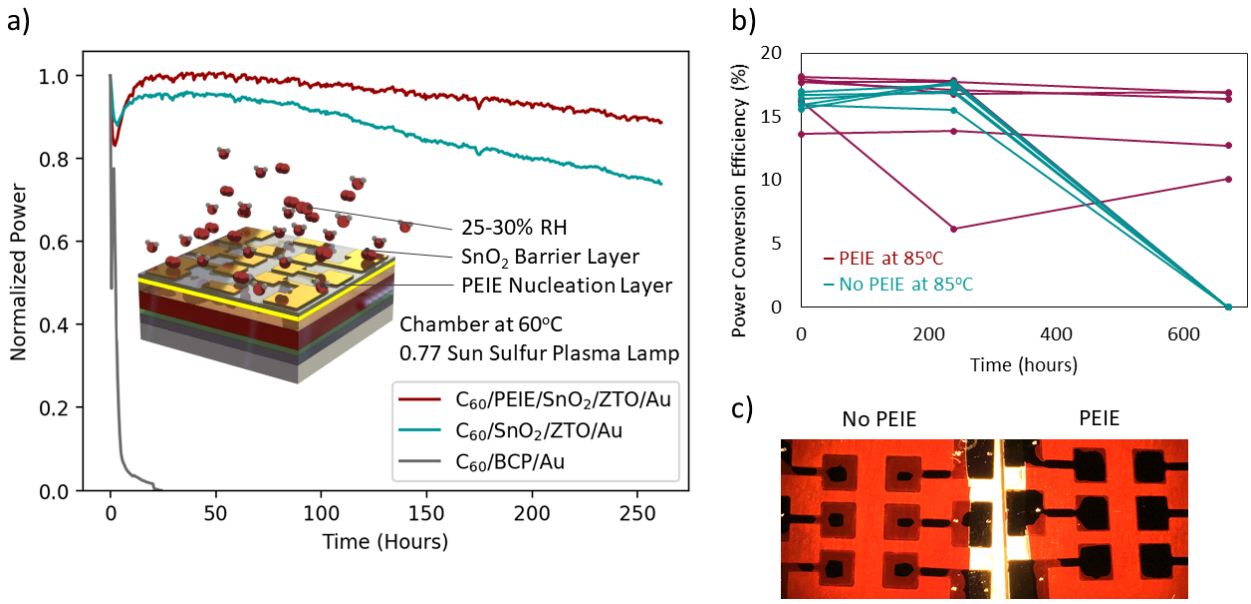

Figure 4: Stability testing of solar cells with and without PEIE nucleation layers. (a) Normalized power of champion unencapsulated $Cs_{0.25}FA_{0.75}Pb(Br_{0.20}I_{0.80})_3$ solar cells with various top contacts (C_{60}/PEIE/SnO_2/ZTO/Au, C_{60}/SnO_2/ZTO/Au, and the more common C_{60}/BCP/Au layer with no SnO_2) over 250 hours under harsh testing conditions of ~0.77 sun illumination, 60°C, and a relative humidity between 25-30%. The device with PEIE retains >90% of its initial efficiency, showing a good improvement over cells without a nucleation layer and a drastic improvement over cells with the organic C_{60}/BCP layers only. Statistics for 8 cells held at maximum power and 50 cells held at open circuit with and without the PEIE nucleation layer are shown in Table 2 and Figure S15. (b) Power conversion efficiency over 670 hours of cells with Ag contacts kept on a hotplate at 85°C in N_2. Each series of points corresponds to the measured efficiency of an individual cell. Traces act as a guide to the eye only. The cells without a PEIE nucleation layer completely lose their initial efficiency as a result of severe metal-halide reactions, as shown in the photographs in (c). The light regions on the metal pixels in (c) correspond to areas where the Ag contact corroded due to halides diffusing through the SnO_2 barrier layer.

Table 2: Summary of average efficiencies remaining with standard deviations of cells tested for 250 hours under illumination at 60°C in ambient air. Devices with PEIE show reproducible stability performance, while devices without PEIE have large standard deviations due to some of them failing completely.

	Held at Maximum Power		Held at Open Circuit	
Device	# Cells	Avg. Power Remaining [%]	# Cells	Avg. Power Remaining [%]
0.025wt% PEIE	4	81.5 ± 9.7	25	60.4 ± 10.8
No PEIE	4	58.5 ± 31.0	25	23.1 ± 24.7

The rigorous stability tests used here expose the perovskite active layer to a variety of known stressors, including the ingress of moisture, oxygen, and reactive metal species and the egress of volatile halide species, all of which have been shown to be mitigated through tailored barrier layers.[1,16,22] While we cannot say for sure which is the limiting factor in this study, it is likely that all of these degradation mechanisms are occurring simultaneously, indicating that the nucleation-enhanced barrier layer here is useful in preventing most or all of these degradation mechanisms. Better nucleation may be beneficial for two reasons: 1) quicker growth of the ALD SnO_2 during deposition prevents ALD precursor diffusion to the perovskite surface where it can degrade the perovskite during cell fabrication, creating defective regions that may further degrade during stability testing, and 2) nucleation on PEIE allows for a thinner, more continuous ALD SnO_2 layer that improves stability without compromising electrical properties. These tests confirm the importance of enhanced nucleation on the effectiveness of ALD barrier layers to prevent degradation of perovskite solar cells under operational conditions and highlight the ability of high-performance perovskite solar cells to exhibit impressive stability. In addition, the large number of devices tested indicates the reproducibility and high yield of this technique in enabling highly-efficient, stable devices.

Conclusions

Atomic layer deposition provides an exciting opportunity for functional barrier layers in perovskite solar cells, and ALD layers have already proven critical in enabling perovskite-perovskite, perovskite-silicon, and perovskite-CIGS tandems. The addition of an ALD SnO_2 contact layer as a 'built-in' barrier layer dramatically improves device stability over typical p-i-n

devices with only organic electron transport layers. We have shown that ALD nucleation is highly dependent on the chemical nature of the underlying surface. We have also demonstrated that the use of a thin, interfacial PEIE nucleation layer can modify existing organic surfaces to improve ALD barrier properties without sacrificing device efficiency. This strategy suppresses internal and external degradation pathways such as: 1) ingress of oxygen, moisture, and reactive metals into the perovskite active layer and 2) migration of mobile halide ion species and degradation products to contacts where they can react, causing both an increase in defects within the active layer and degradation of the contacts themselves. The design and understanding of nucleation and growth of barrier layers within perovskite optoelectronic devices opens a new path towards improvement of stability for this promising technology.

Experimental Section

Auger electron spectroscopy: AES mapping was performed on a PHI 700 Scanning Auger Nanoprobe instrument with a 10keV/10nA primary electron beam and 128x128 pixel resolution.

Absorption measurements: Absorption measurements were taken on a Jasco Model V-670 UV-Vis-NIR spectrometer with a 60 mm integrating sphere at a scan speed of 2000 nm/min.

Spectroscopy ellipsometry: Film thicknesses of the PEIE and ALD SnO_2 layers were determined by spectroscopic ellipsometry measurements taken on a J.A. Woollam Co., Inc. α SE ellipsometer at incident light angles of 65° and 70° over a 380-900 nm wavelength range. CompleteEASE software from J.A. Woollam was used to fit the ellipsometry data. Polished silicon substrates were used for the ALD SnO_2 films. The ALD SnO_2 data was fit with a simple Cauchy film model. PEIE thickness was measured on top of C_{60} on a polished silicon substrate. The C_{60} layer was fit with two Tauc-Lorentz oscillators[68] and the PEIE layer was fit with a separate Cauchy film model. Representative ellipsometry data for C_{60}/PEIE films is shown in Figure S4. Fit parameters of the Tauc-Lorentz oscillators for C_{60} and the Cauchy equations (Equations S1 and S2) for PEIE are listed in Table S1 and S2, respectively. Optical constants of C_{60} and PEIE extracted from the models are shown in Figure S5.

X-ray photoelectron spectroscopy: XPS measurements were taken on a PHI VersaProbe 3 system with Al Kα (1486 eV) radiation, a 200 µm beam size, 50 W beam power and 15 kV e-beam energy. A 0.5 kV x 0.6 µA Ar^+ focused ion gun was used for depth profile sputtering. The XPS data was fit using Multipak software (Copyright 2019, Physical Electronics, Inc.).

Perovskite precursor: Formamidinium iodide (GreatCell Solar), cesium iodide (Sigma Aldrich), lead (II) bromide (Sigma Aldrich), and lead (II) iodide (TCI America) powders were

weighed out at a stoichiometric ratio of $Cs_{0.25}FA_{0.75}Pb(Br_{0.20}I_{0.80})_3$ and ball-milled together into a powder. A small amount (2 mol%) of stoichiometric excess lead (II) chloride (Alfa Aesar) was added to the powder just before dissolving at 1.4M in N,N-dimethylformamide (DMF, Sigma Aldrich) and dimethylsulfoxide (DMSO, Sigma Aldrich) at a volume ratio of 3:1.

Perovskite solar cell fabrication: ITO-patterned, 15 ohm/sq., 2.5cm x 2.5cm x 1mm ITO-glass substrates from Xin Yan Technology were sequentially cleaned in an ultrasonic bath with acetone followed by isopropanol for 15 minutes each. They were then UV-ozone cleaned for 15 minutes prior to subsequent film deposition, which was done in a nitrogen glovebox. Poly-TPD (poly(4-butylphenyl-diphenyl-amine), 1-Material), was dissolved at 1 mg/mL in chlorobenzene and dynamically spun by dripping 70 uL onto a substrate spinning at 4000 rpm with 30 seconds remaining in the spin cycle. Following deposition, substrates were annealed at 110ºC for 10 minutes and then allowed to cool back to room temperature. 65 µL of PFN-Br (poly[(9,9-bis(3'-((N,N-dimethyl)-N-ethylammonium)-propyl)-2,7-fluorene)-alt-2,7-(9,9-dioctylfluorene)], 1-Material) dissolved in methanol 0.5 mg/mL was dripped into a substrate spinning at 5000 rpm with 25 seconds remaining in the spin cycle. Immediately after PFN deposition, 40 µL of perovskite solution was spread onto the substrate and spun at 5000 rpm for 50s. 400 µL of methyl acetate was dripped onto the spinning substrate with 25 seconds remaining in the spin cycle, and the perovskite film was annealed at 85ºC for 1 minute followed by 100ºC for 30 minutes. Poly-TPD, PFN, and the perovskite were all spun using a Laurell WS-650-23B spincoater. 1 nm of LiF (Kurt J. Lesker) at a rate of 0.1 Å/s and 30 nm of C_{60} (Lumtec) at a rate of 0.2 Å/s for the first 5 nm and 0.5 Å/s for the remaining 25 nm were deposited via thermal evaporation in an Angstrom evaporator. For the control, opaque solar cells without SnO_2 barrier layers, 6 nm of bathocuproine (BCP, Sigma Aldrich) was deposited via thermal evaporation at a

rate of 0.2 Å/s, followed by 120 nm of Au (Kurt J. Lesker) at a rate of 0.5 Å/s for the first 5 nm followed by a rate of 2 Å/s for the remaining 115 nm. For the devices with the nucleation layer, PEIE (polyethylenimine, 80% ethoxylated solution, 35-40 wt. % in H_2O, M_W 110,000, Sigma Aldrich) was diluted to 0.1 wt. % in isopropanol in a stock solution, followed by a further dilution to 0.025 wt. % or 0.05 wt. % in isopropanol. The dilute solution in IPA was dropped onto the perovskite surface while the substrate was stationary and spun at 5000 rpm for 20s using a Specialty Coating Systems Inc. G3P-12 spincoater with an acceleration time of 1 second, followed by an anneal at 100ºC for 2 minutes. Atomic layer deposition of SnO_2/ZTO was performed as reported elsewhere.[32,56] Devices were completed via thermal evaporation of Au contacts in an Angstrom evaporator.

Current-voltage measurements: JV measurements were taken in a nitrogen glovebox using an Oriel 94043A Sol3A Class AAA solar simulator from Newport calibrated to 1-sun intensity with a silicon photodiode with a KG2 filter. Devices were shadow masked using a 0.058 cm^2 aperture. External quantum efficiency (EQE) measurements were measured using an ORIEL IQE 200 solar cell quantum-efficiency measurement system from Newport.

Lifetime testing: Stability testing was done on a multi-channel, custom-built setup that allowed for simultaneous maximum power point tracking of each individual cell. The initial maximum power voltage was determined by a JV sweep, after which the maximum power point was achieved by holding each cell at a specific voltage and measuring the resulting current. The voltage was updated every 2 seconds using a perturb and observe algorithm to optimize maximum power output. A JV sweep was taken every 5 hours from short circuit to open circuit. The cells were aged in a covered chamber exposed to ambient air. An LG Plasma Lighting Systems PSH0731B sulfur-plasma lamp was used to illuminate the samples at approximately

0.77 suns. The lamp spectrum is shown in Figure S13. Lamp intensity was monitored throughout the duration of the aging test using silicon photodiodes spaced throughout the chamber. No significant changes in intensity were measured during the duration of the test. For details on each tracked cell see the attached ISOS Protocols Data Collection worksheet.

Supporting Information
Supporting Information is available from the Wiley Online Library or from the author.

Acknowledgements
J.A.R and C.C.B contributed equally to this work. This work is supported by the U.S. Department of Energy (DOE) Office of Energy Efficiency and Renewable Energy (EERE) under Solar Energy Technologies Office (SETO) Agreement Number DE-EE0008167. C.C.B. acknowledges support from the National Science Foundation Graduate Research Fellowship under Grant No. DGE-1656518. Work at the National Renewable Energy Laboratory is supported by the US DOE under Contract Number DE-AC36-08GO23808. A.F.P. acknowledges support from the De-risking halide perovskite solar cells program of the National Center for Photovoltaics, also funded by the US DOE, Office of EERE under SETO. E.J.W. acknowledges support from the Office of Naval Research under award number N00014-17-1-2525. Part of this work was performed at the Stanford Nano Shared Facilities (SNSF) and the Stanford Nanofabrication Facility (SNF), supported by the National Science Foundation under award ECCS-1542152. The authors would like to thank Yunzhi Liu and Joonsuk Park for electron microscopy characterization.

References

[1] C. C. Boyd, R. Cheacharoen, T. Leijtens, M. D. McGehee, C., R. Cheacharoen, T. Leijtens, M. D. McGehee, *Chem. Rev.* **2019**, *119*, 3418.
[2] T. Leijtens, G. E. Eperon, N. K. Noel, S. N. Habisreutinger, A. Petrozza, H. J. Snaith, *Adv. Energy Mater.* **2015**, *5*, 1500963.
[3] T. A. Berhe, W.-N. Su, C.-H. Chen, C.-J. Pan, J.-H. Cheng, H.-M. Chen, M.-C. Tsai, L.-Y. Chen, A. A. Dubale, B.-J. Hwang, *Energy Environ. Sci.* **2016**, *9*, 323.
[4] R. Wang, M. Mujahid, Y. Duan, Z.-K. Wang, J. Xue, Y. Yang, *Adv. Funct. Mater.* **2019**, 1808843.
[5] M. I. Saidaminov, J. Kim, A. Jain, R. Quintero-Bermudez, H. Tan, G. Long, F. Tan, A. Johnston, Y. Zhao, O. Voznyy, E. H. Sargent, *Nat. Energy* **2018**, *3*, 648.
[6] K. A. Bush, K. Frohna, R. Prasanna, R. E. Beal, T. Leijtens, S. A. Swifter, M. D. McGehee, *ACS Energy Lett* **2018**, *3*, 428.
[7] Z. Wang, Z. Shi, T. Li, Y. Chen, W. Huang, *Angew. Chemie Int. Ed.* **2017**, *56*, 1190.
[8] S.-H. Turren-Cruz, A. Hagfeldt, M. Saliba, *Science* **2018**, *362*, 449.
[9] M. Saliba, T. Matsui, J.-Y. Seo, K. Domanski, J.-P. Correa-Baena, M. K. Nazeeruddin, S. M. Zakeeruddin, W. Tress, A. Abate, A. Hagfeldt, M. Grätzel, *Energy Environ. Sci.* **2016**,

9, 1989.
[10] D. P. McMeekin, G. Sadoughi, W. Rehman, G. E. Eperon, M. Saliba, M. T. Hörantner, A. Haghighirad, N. Sakai, L. Korte, B. Rech, M. B. Johnston, L. M. Herz, H. J. Snaith, *Science* **2016**, *351*, 151.
[11] A. Mei, X. Li, L. Liu, Z. Ku, T. Liu, Y. Rong, M. Xu, M. Hu, J. Chen, Y. Yang, M. Grätzel, H. Han, *Science* **2014**, *345*, 295.
[12] S. Seo, S. Jeong, C. Bae, N.-G. Park, H. Shin, *Adv. Mater.* **2018**, *30*, 1801010.
[13] M. Kaltenbrunner, G. Adam, E. D. Głowacki, M. Drack, R. Schwödiauer, L. Leonat, D. H. Apaydin, H. Groiss, M. C. Scharber, M. S. White, N. S. Sariciftci, S. Bauer, *Nat. Mater.* **2015**, *14*, 1032.
[14] G. Grancini, C. Roldán-Carmona, I. Zimmermann, E. Mosconi, X. Lee, D. Martineau, S. Narbey, F. Oswald, F. De Angelis, M. Graetzel, M. K. Nazeeruddin, *Nat. Commun.* **2017**, *8*, 15684.
[15] K. O. Brinkmann, J. Zhao, N. Pourdavoud, T. Becker, T. Hu, S. Olthof, K. Meerholz, L. Hoffmann, T. Gahlmann, R. Heiderhoff, M. F. Oszajca, N. A. Luechinger, D. Rogalla, Y. Chen, B. Cheng, T. Riedl, *Nat. Commun.* **2017**, *8*, 13938.
[16] J. A. Christians, P. Schulz, J. S. Tinkham, T. H. Schloemer, S. P. Harvey, B. J. Tremolet de Villers, A. Sellinger, J. J. Berry, J. M. Luther, *Nat. Energy* **2018**, *3*, 68.
[17] T. Leijtens, G. E. Eperon, S. Pathak, A. Abate, M. M. Lee, H. J. Snaith, *Nat. Commun.* **2013**, *4*, 2885.
[18] T. Leijtens, T. Giovenzana, S. N. Habisreutinger, J. S. Tinkham, N. K. Noel, B. A. Kamino, G. Sadoughi, A. Sellinger, H. J. Snaith, *ACS Appl. Mater. Interfaces* **2016**, *8*, 5981.
[19] D. Koushik, W. J. H. Verhees, Y. Kuang, S. Veenstra, D. Zhang, M. A. Verheijen, M. Creatore, R. E. I. Schropp, *Energy Environ. Sci.* **2017**, *10*, 91.
[20] K. A. Bush, C. D. Bailie, Y. Chen, A. R. Bowring, W. Wang, W. Ma, T. Leijtens, F. Moghadam, M. D. McGehee, *Adv. Mater.* **2016**, *28*, 3937.
[21] X. Zheng, B. Chen, J. Dai, Y. Fang, Y. Bai, Y. Lin, H. Wei, X. C. Zeng, J. Huang, *Nat. Energy* **2017**, *2*, 17102.
[22] C. C. Boyd, R. Cheacharoen, K. A. Bush, R. Prasanna, T. Leijtens, M. D. McGehee, *ACS Energy Lett.* **2018**, *3*, 1772.
[23] M. Abdi-Jalebi, Z. Andaji-Garmaroudi, S. Cacovich, C. Stavrakas, B. Philippe, J. M. Richter, M. Alsari, E. P. Booker, E. M. Hutter, A. J. Pearson, S. Lilliu, T. J. Savenije, H. Rensmo, G. Divitini, C. Ducati, R. H. Friend, S. D. Stranks, *Nature* **2018**, *555*, 497.
[24] F. Bella, G. Griffini, J.-P. Correa-Baena, G. Saracco, M. Grätzel, A. Hagfeldt, S. Turri, C. Gerbaldi, *Science* **2016**, *354*, 203.
[25] R. Cheacharoen, C. C. Boyd, G. F. Burkhard, T. Leijtens, J. A. Raiford, K. A. Bush, S. F. Bent, M. D. McGehee, *Sustain. Energy Fuels* **2018**, *2*, 2398.
[26] S. Seo, S. Jeong, H. Park, H. Shin, N.-G. Park, *Chem. Commun.* **2019**, *55*, 2403.
[27] V. Zardetto, B. L. Williams, A. Perrotta, F. Di Giacomo, M. A. Verheijen, R. Andriessen, W. M. M. Kessels, M. Creatore, *Sustain. Energy Fuels* **2017**, *1*, 30.
[28] A. F. Palmstrom, G. E. Eperon, T. Leijtens, R. Prasanna, S. N. Habisreutinger, W. Nemeth, E. A. Gaulding, S. P. Dunfield, M. Reese, S. Nanayakkara, T. Moot, J. Werner, J. Liu, B. To, S. T. Christensen, M. D. McGehee, M. F. A. M. van Hest, J. M. Luther, J. J. Berry, D. T. Moore, *Joule* **2019**, DOI 10.1016/j.joule.2019.05.009.
[29] J. Tong, Z. Song, D. H. Kim, X. Chen, C. Chen, A. F. Palmstrom, P. F. Ndione, M. O.

Reese, S. P. Dunfield, O. G. Reid, J. Liu, F. Zhang, S. P. Harvey, Z. Li, S. T. Christensen, G. Teeter, D. Zhao, M. M. Al-Jassim, M. F. A. M. van Hest, M. C. Beard, S. E. Shaheen, J. J. Berry, Y. Yan, K. Zhu, *Science* **2019**, *364*, 475.
[30] G. E. Eperon, T. Leijtens, K. A. Bush, R. Prasanna, T. Green, J. T.-W. Wang, D. P. McMeekin, G. Volonakis, R. L. Milot, R. May, A. Palmstrom, D. J. Slotcavage, R. A. Belisle, J. B. Patel, E. S. Parrott, R. J. Sutton, W. Ma, F. Moghadam, B. Conings, A. Babayigit, H.-G. Boyen, S. Bent, F. Giustino, L. M. Herz, M. B. Johnston, M. D. McGehee, H. J. Snaith, *Science* **2016**, *354*, 861.
[31] K. A. Bush, S. Manzoor, K. Frohna, Z. J. Yu, J. A. Raiford, A. F. Palmstrom, H. P. Wang, R. Prasanna, S. F. Bent, Z. C. Holman, M. D. McGehee, *ACS Energy Lett.* **2018**, *3*, 2173.
[32] K. A. Bush, A. F. Palmstrom, Z. J. Yu, M. Boccard, R. Cheacharoen, J. P. Mailoa, D. P. McMeekin, R. L. Z. Hoye, C. D. Bailie, T. Leijtens, I. M. Peters, M. C. Minichetti, N. Rolston, R. Prasanna, S. Sofia, D. Harwood, W. Ma, F. Moghadam, H. J. Snaith, T. Buonassisi, Z. C. Holman, S. F. Bent, M. D. McGehee, *Nat. Energy* **2017**, *2*, 17009.
[33] B. Chen, Z. Yu, K. Liu, X. Zheng, Y. Liu, J. Shi, D. Spronk, P. N. Rudd, Z. Holman, J. Huang, *Joule* **2019**, *3*, 177.
[34] M. Jošt, E. Köhnen, A. B. Morales-Vilches, B. Lipovšek, K. Jäger, B. Macco, A. Al-Ashouri, J. Krč, L. Korte, B. Rech, R. Schlatmann, M. Topič, B. Stannowski, S. Albrecht, *Energy Environ. Sci.* **2018**, *11*, 3511.
[35] F. Sahli, J. Werner, B. A. Kamino, M. Bräuninger, R. Monnard, B. Paviet-Salomon, L. Barraud, L. Ding, J. J. Diaz Leon, D. Sacchetto, G. Cattaneo, M. Despeisse, M. Boccard, S. Nicolay, Q. Jeangros, B. Niesen, C. Ballif, *Nat. Mater.* **2018**, *17*, 820.
[36] M. Jošt, T. Bertram, D. Koushik, J. A. Marquez, M. A. Verheijen, M. D. Heinemann, E. Köhnen, A. Al-Ashouri, S. Braunger, F. Lang, B. Rech, T. Unold, M. Creatore, I. Lauermann, C. A. Kaufmann, R. Schlatmann, S. Albrecht, *ACS Energy Lett.* **2019**, *4*, 583.
[37] H. C. Guo, Z. Li, M.-Y. Han, *Mater. Sci. Eng. C* **2017**, *70*, 1182.
[38] G. N. Parsons, *Atomic Layer Deposition of Nanostructured Materials*, Wiley-VCH/Verlag GmbH & Co. KGaA, **2012**.
[39] G. N. Parsons, S. E. Atanasov, E. C. Dandley, C. K. Devine, B. Gong, J. S. Jur, K. Lee, C. J. Oldham, Q. Peng, J. C. Spagnola, P. S. Williams, *Coord. Chem. Rev.* **2013**, *257*, 3323.
[40] Y. Xu, C. B. Musgrave, *Chem. Mater.* **2004**, *16*, 646.
[41] B. Gong, G. N. Parsons, *J. Mater. Chem.* **2012**, *22*, 15672.
[42] J. C. Spagnola, B. Gong, S. A. Arvidson, J. S. Jur, S. A. Khan, G. N. Parsons, *J. Mater. Chem.* **2010**, *20*, 4213.
[43] J. S. Jur, J. C. Spagnola, K. Lee, B. Gong, Q. Peng, G. N. Parsons, *Langmuir* **2010**, *26*, 8239.
[44] M. Kemell, V. Pore, M. Ritala, M. Leskelä, M. Lindén, *J. Am. Chem. Soc.* **2005**, *127*, 14178.
[45] Q. Peng, X.-Y. Sun, J. C. Spagnola, G. K. Hyde, R. J. Spontak, G. N. Parsons, *Nano Lett.* **2007**, *7*, 719.
[46] Y. Zhou, C. Fuentes-Hernandez, J. W. Shim, T. M. Khan, B. Kippelen, *Energy Environ. Sci.* **2012**, *5*, 9827.
[47] E. Saracco, B. Bouthinon, J.-M. Verilhac, C. Celle, N. Chevalier, D. Mariolle, O. Dhez, J.-P. Simonato, *Adv. Mater.* **2013**, *25*, 6534.
[48] L. Yan, Y. Song, Y. Zhou, B. Song, Y. Li, *Org. Electron.* **2015**, *17*, 94.
[49] H. Yang, J. Zhang, C. Zhang, J. Chang, Z. Lin, D. Chen, X. Sun, H. Xi, G. Han, Y. Hao,

Sol. Energy **2016**, *139*, 190.
[50] H. Zhou, Q. Chen, G. Li, S. Luo, T. Song, H.-S. Duan, Z. Hong, J. You, Y. Liu, Y. Yang, *Science* **2014**, *345*, 542.
[51] Y. Zhou, C. Fuentes-Hernandez, J. Shim, J. Meyer, A. J. Giordano, H. Li, P. Winget, T. Papadopoulos, H. Cheun, J. Kim, M. Fenoll, A. Dindar, W. Haske, E. Najafabadi, T. M. Khan, H. Sojoudi, S. Barlow, S. Graham, J.-L. Brédas, S. R. Marder, A. Kahn, B. Kippelen, *Science* **2012**, *336*, 327.
[52] O. Malinkiewicz, A. Yella, Y. H. Lee, G. M. Espallargas, M. Graetzel, M. K. Nazeeruddin, H. J. Bolink, *Nat. Photonics* **2014**, *8*, 128.
[53] K. Wojciechowski, T. Leijtens, S. Siprova, C. Schlueter, M. T. Hörantner, J. T.-W. Wang, C.-Z. Li, A. K.-Y. Jen, T.-L. Lee, H. J. Snaith, *J. Phys. Chem. Lett.* **2015**, *6*, 2399.
[54] Y. Shao, Z. Xiao, C. Bi, Y. Yuan, J. Huang, *Nat. Commun.* **2014**, *5*, 5784.
[55] X. Yu, H. Yan, Q. Peng, *Langmuir* **2019**, *35*, 6522.
[56] A. F. Palmstrom, J. A. Raiford, R. Prasanna, K. A. Bush, M. Sponseller, R. Cheacharoen, M. C. Minichetti, D. S. Bergsman, T. Leijtens, H. Wang, V. Bulovic, M. D. Mcgehee, S. F. Bent, *Adv. Energy Mater.* **2018**, *8*, 1800591.
[57] D. Koushik, L. Hazendonk, V. Zardetto, V. Vandalon, M. A. Verheijen, W. M. M. Kessels, M. Creatore, *ACS Appl. Mater. Interfaces* **2019**, *11*, 5526.
[58] D. Choudhury, G. Rajaraman, S. K. Sarkar, *Nanoscale* **2016**, *8*, 7459.
[59] S. Chu, R. Zhao, R. Liu, Y. Gao, X. Wang, C. Liu, J. Chen, H. Zhou, *Semicond. Sci. Technol.* **2018**, *33*, 115016.
[60] J. A. Raiford, R. A. Belisle, K. A. Bush, R. Prasanna, A. F. Palmstrom, M. D. McGehee, S. F. Bent, *Sustain. Energy Fuels* **2019**, *3*, 1517.
[61] M. Stolterfoht, C. M. Wolff, J. A. Márquez, S. Zhang, C. J. Hages, D. Rothhardt, S. Albrecht, P. L. Burn, P. Meredith, T. Unold, D. Neher, *Nat. Energy* **2018**, *3*, 847.
[62] N. Li, S. Tao, Y. Chen, X. Niu, C. K. Onwudinanti, C. Hu, Z. Qiu, Z. Xu, G. Zheng, L. Wang, Y. Zhang, L. Li, H. Liu, Y. Lun, J. Hong, X. Wang, Y. Liu, H. Xie, Y. Gao, Y. Bai, S. Yang, G. Brocks, Q. Chen, H. Zhou, *Nat. Energy* **2019**, *4*, 408.
[63] P. Holzhey, M. Saliba, *J. Mater. Chem. A* **2018**, *6*, 21794.
[64] K. Domanski, J.-P. Correa-Baena, N. Mine, M. K. Nazeeruddin, A. Abate, M. Saliba, W. Tress, A. Hagfeldt, M. Grätzel, *ACS Nano* **2016**, *10*, 6306.
[65] N. N. Shlenskaya, N. A. Belich, M. Grätzel, E. A. Goodilin, A. B. Tarasov, *J. Mater. Chem. A* **2018**, *6*, 1780.
[66] R. A. Kerner, P. Schulz, J. A. Christians, S. P. Dunfield, B. Dou, L. Zhao, G. Teeter, J. J. Berry, B. P. Rand, *APL Mater.* **2019**, *7*, 041103.
[67] B. Chen, J. Song, X. Dai, Y. Liu, P. N. Rudd, X. Hong, J. Huang, *Adv. Mater.* **2019**, 1902413.
[68] G. E. Jellison, F.A. Modine, *Appl. Phys. Lett.* **1996**, *69*, 371.

Table of Contents

An ultra-thin functional polymer layer is used to enhance the nucleation of atomic layer deposited (ALD) SnO_2 contacts in metal-halide perovskite solar cells. These nucleation-enhanced ALD layers act as 'built-in' barriers to both internal and external degradation pathways, significantly improving the long-term operational stability of high efficiency unencapsulated devices (>18%) in air.

Keyword: Perovskite Solar Cells

J. A. Raiford, C. C. Boyd, A. F. Palmstrom, E. J. Wolf, B. A. Fearon, J. J. Berry, M. D. McGehee, S. F. Bent*

Enhanced Nucleation of Atomic Layer Deposited Contacts Improves Operational Stability of Perovskite Solar Cells in Air

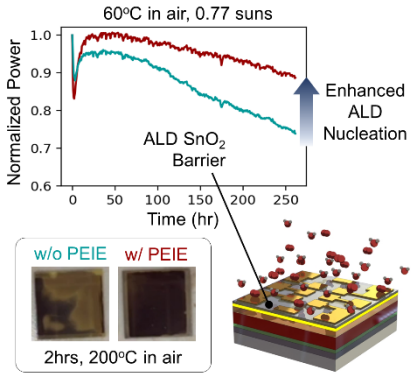

Supporting Information

Enhanced Nucleation of Atomic Layer Deposited Contacts Improves Operational Stability of Perovskite Solar Cells in Air

James A. Raiford, Caleb C. Boyd, Axel F. Palmstrom, Eli J. Wolf, Benjamin A. Fearon, Joseph J. Berry, Michael D. McGehee, Stacey F. Bent*

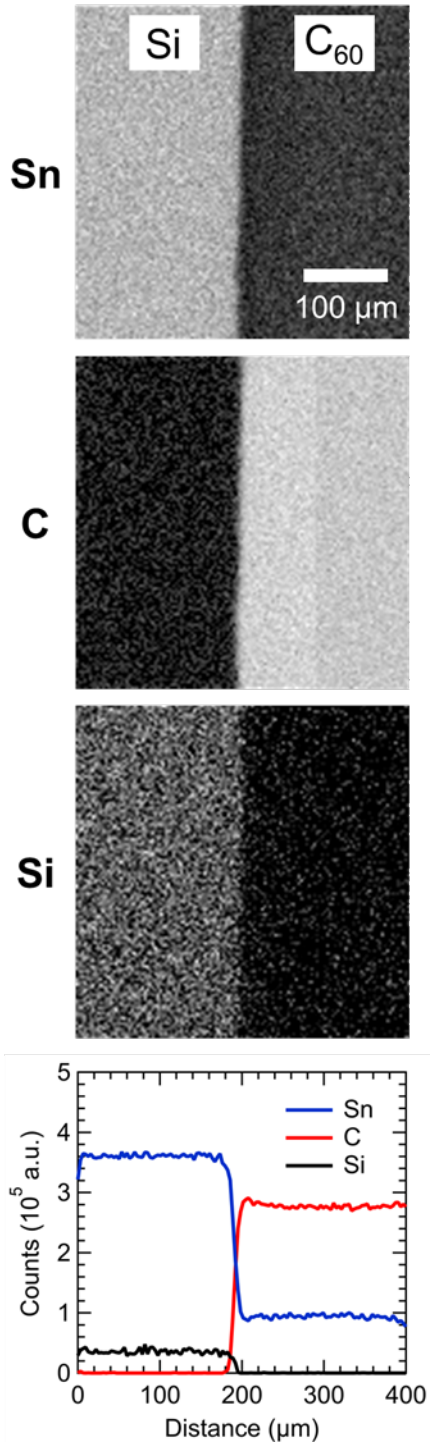

Figure S1: Tin, carbon, and silicon elemental maps by Auger electron spectroscopy (AES) and the resultant horizontal line scans for 10 cycles of ALD SnO_2 on patterned Si/C_{60} substrates. The brighter pixels represent a higher electron count corresponding to each element.

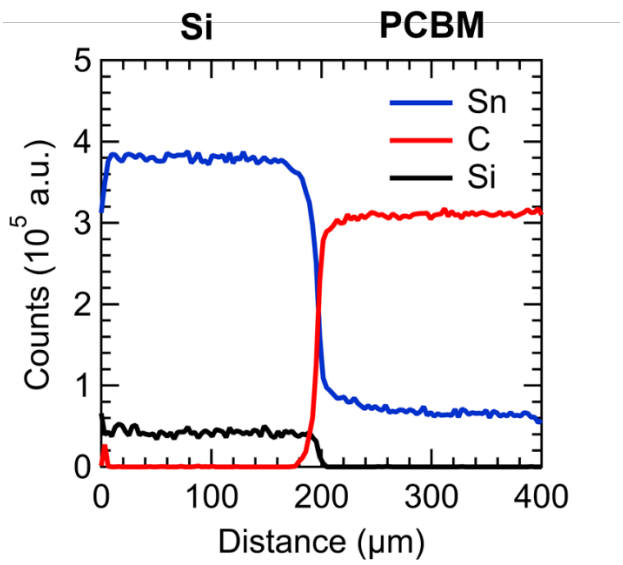

Figure S2: Tin, carbon, and silicon elemental line scans by AES for 10 cycles of ALD SnO_2 on silicon substrates patterned with evaporated PCBM.

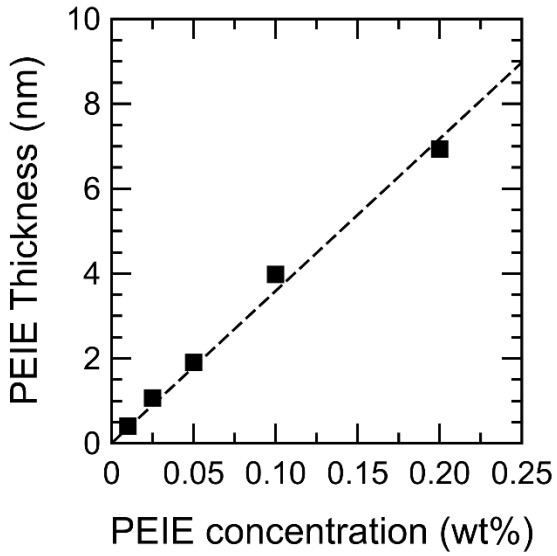

Figure S3: PEIE thickness as a function of solution concentration spun on UV/O_3-cleaned polished silicon. The measured thickness values (squares) were determined by fitting a Cauchy film model to spectroscopic ellipsometry data. The dashed line is a linear fit to the data with a fixed y-intercept at the origin.

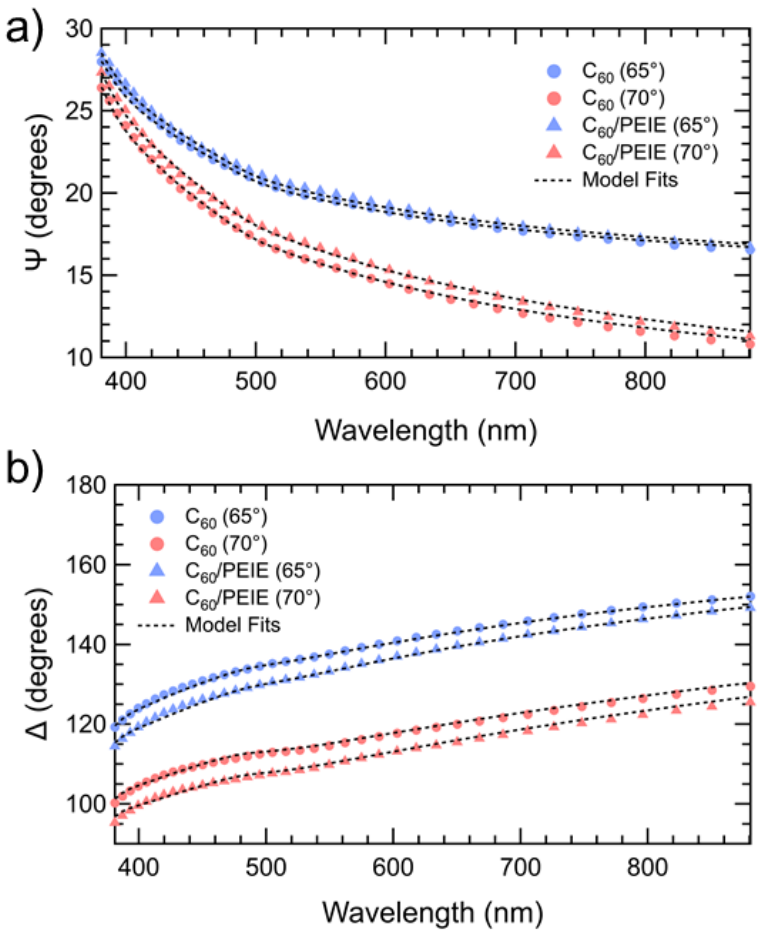

Figure S4: (a) Amplitude ratio (Ψ) and (b) phase difference (Δ) as a function of wavelength measured by spectroscopic ellipsometry of C_{60} and C_{60}/PEIE films on polished silicon substrates. Measurements were taken at two angles of incident light, 65° and 70°. The C_{60} layer was fit with two Tauc-Lorentz oscillators and the PEIE layer was fit with a separate Cauchy film model described below.

Table S1: Tauc-Lorentz oscillator fit parameters for C_{60} from spectroscopic ellipsometry modeling.

Oscillator	E_g (eV)	E_0 (eV)	A (eV)	C (eV)
1	1.284	4.089	15.099	2.690
2	0.987	2.614	0.939	0.393

E_g = band gap energy
E_0 = energy position of peak
A = peak strength
C = peak broadening

Table S2: Cauchy fit parameters and film thickness of PEIE from spectroscopic ellipsometry modeling.

A	B (μm^2)	C (μm^4)	a	k	E_{BE} (eV)	Thickness (nm)
1.125	0.364	-0.0416	0.066	1.562	3.1 (fixed)	2.3

Cauchy equations:

$$(S1) \quad n = A + \frac{B}{\lambda^2} + \frac{C}{\lambda^4}$$

$$(S2) \quad k = ae^{k(E-E_{BE})}$$

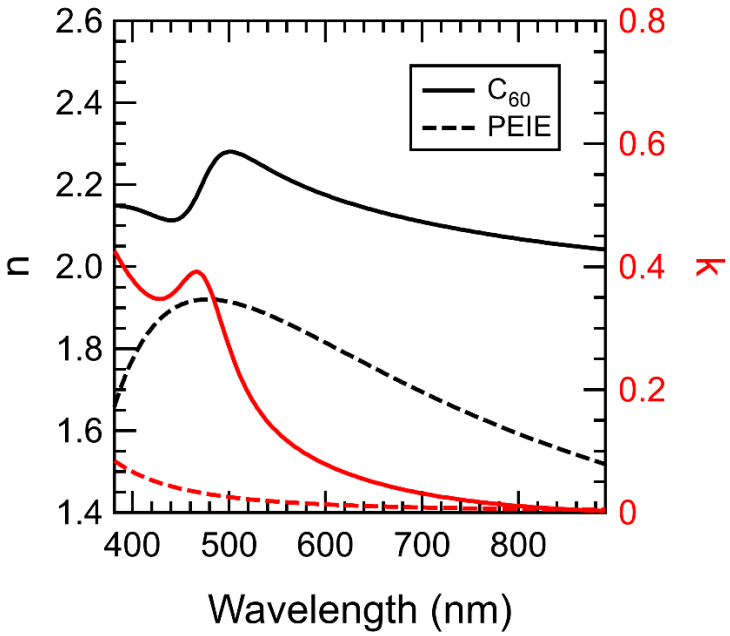

Figure S5: Refractive index (n) and extinction coefficient (k) as a function of wavelength for C_{60} and PEIE extracted from Tauc-Lorentz and Cauchy film models, respectively, used to fit the spectroscopic ellipsometry data shown in Figure S4.

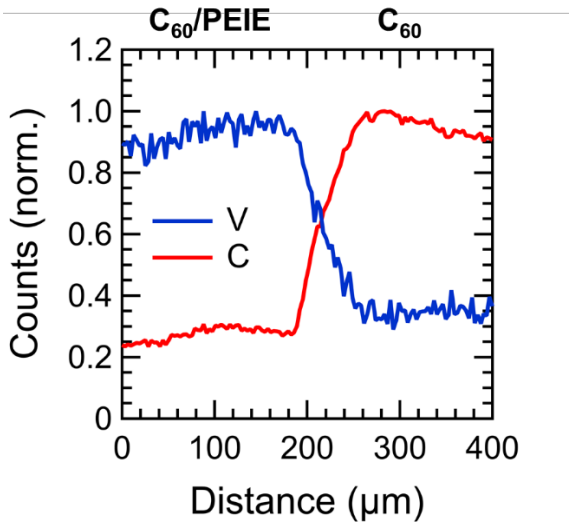

Figure S6: Line scan of elemental vanadium and carbon by AES for 40 cycles of ALD vanadium oxide (grown at 80°C using vanadium(V) oxytriisopropoxide and water) on a C_{60} substrate. The left side of the C_{60} substrate was coated with a thin layer of PEIE (0.025 wt% in IPA) prior to ALD.

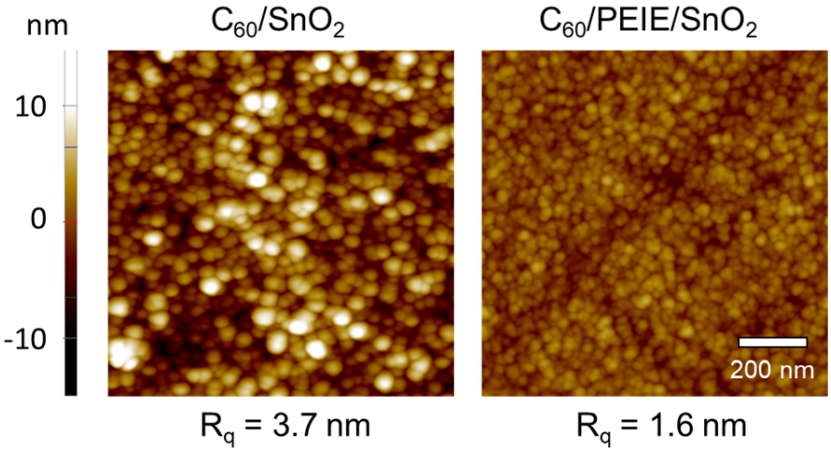

Figure S7: AFM images (1 μm x 1 μm) of 3 nm (15 cycles) of ALD SnO_2 on C_{60} with and without an interfacial PEIE nucleation layer. Root-mean-squared roughness (R_q) values for each surface are included beneath the images.

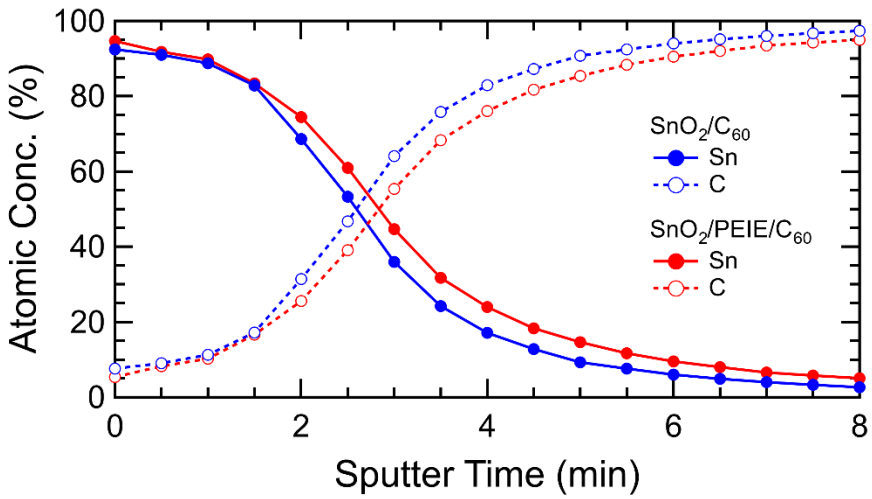

Figure S8: XPS sputter depth profile through the SnO_2/C_{60} interface with and without the PEIE nucleation layer. The relative atomic concentrations of Sn and C were calculated from high resolution spectra of the Sn3d and C1s peaks, respectively.

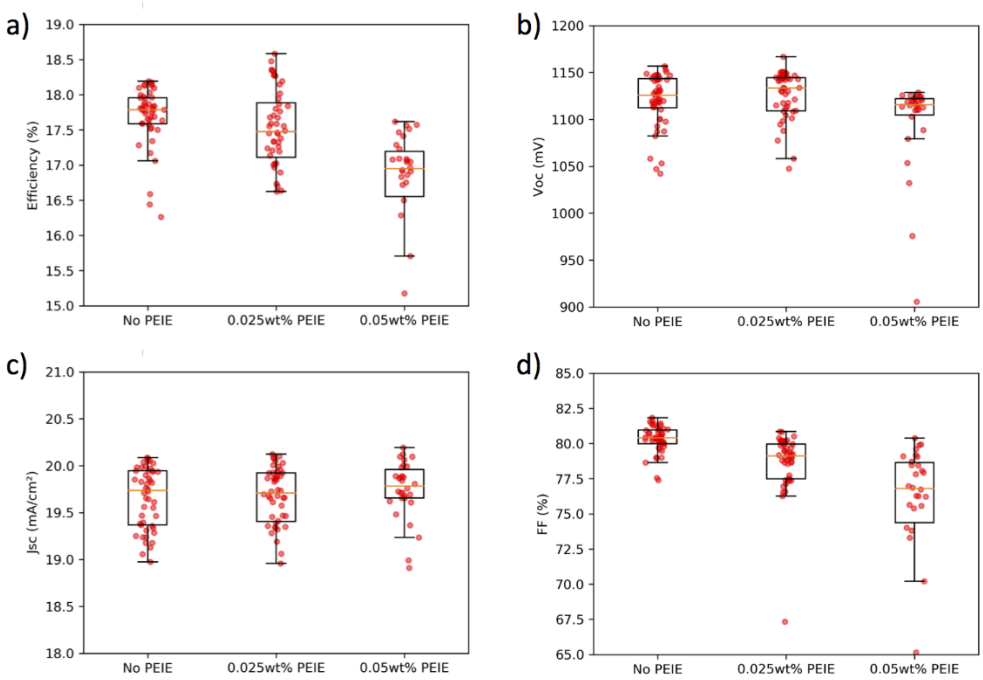

Figure S9: Individual device statistics for p-i-n cells with ITO/poly-TPD/PFN/$FA_{0.75}Cs_{0.25}Pb(I_{0.8}Br_{0.2})_3$/LiF/C60/(0.025wt% PEIE, 0.05wt% PEIE, or No PEIE)/ALD SnO_2/ZTO/Au architectures.

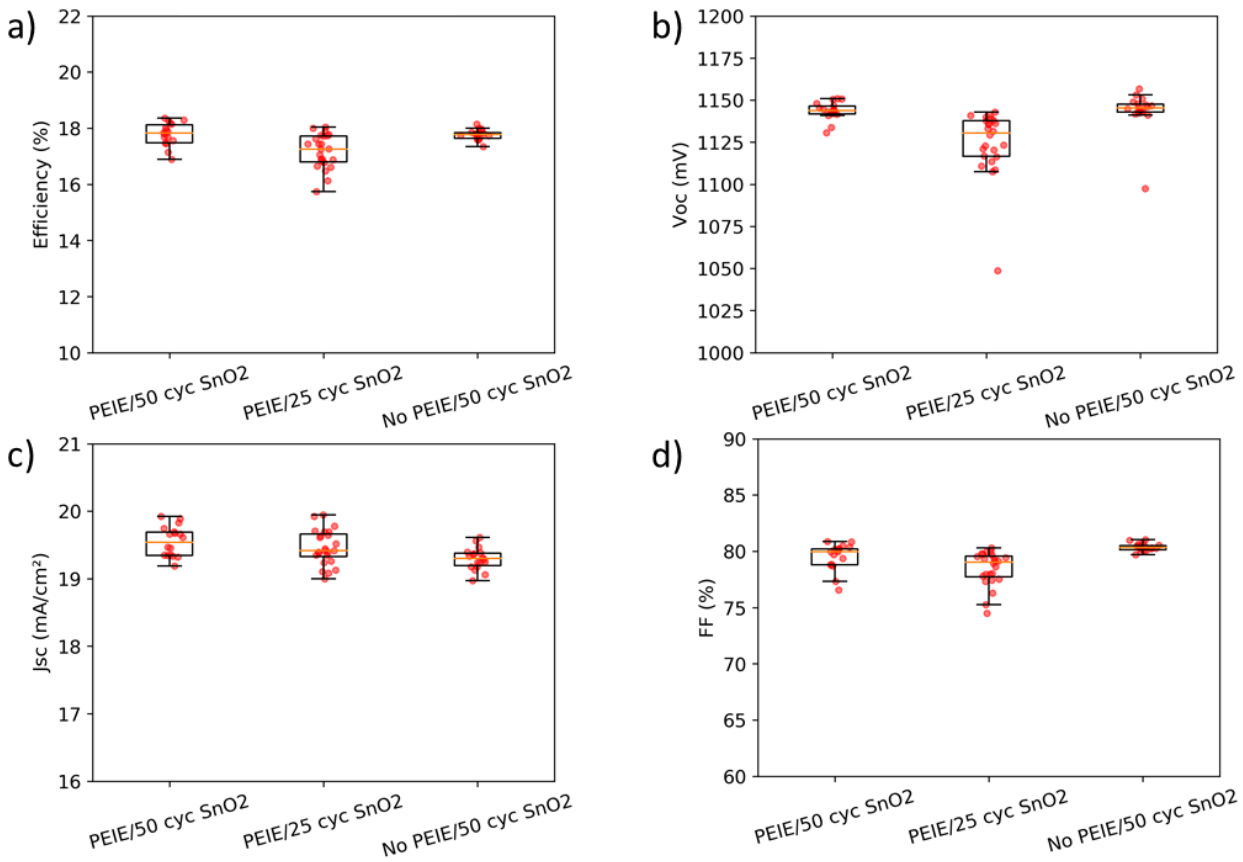

Figure S10: (a) Efficiency, (b) V_{OC}, (c) J_{SC}, and (d) FF statistics for a batch of devices with 50 cycles vs 25 cycles of ALD SnO_2 (both deposited on PEIE nucleation layers) vs control devices with no PEIE and 50 cycles of ALD SnO_2.

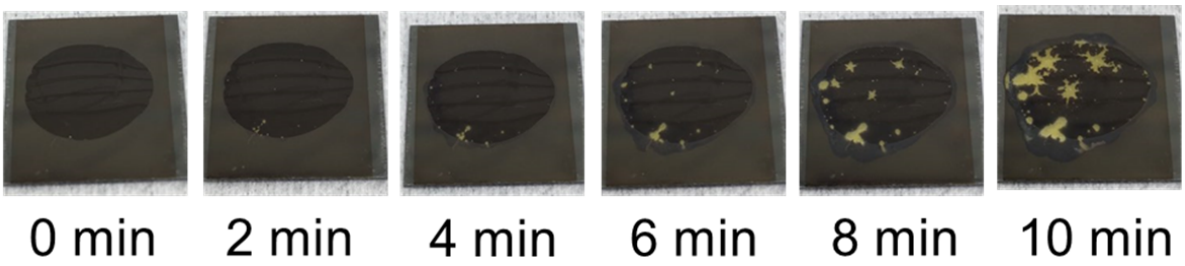

Figure S11: Time lapse images of a $Cs_{0.25}FA_{0.75}Pb(Br_{0.20}I_{0.80})_3/C_{60}$/PEIE/$SnO_2$ (25 cycles) sample exposed to a drop of water on the SnO_2 surface for 10 minutes.

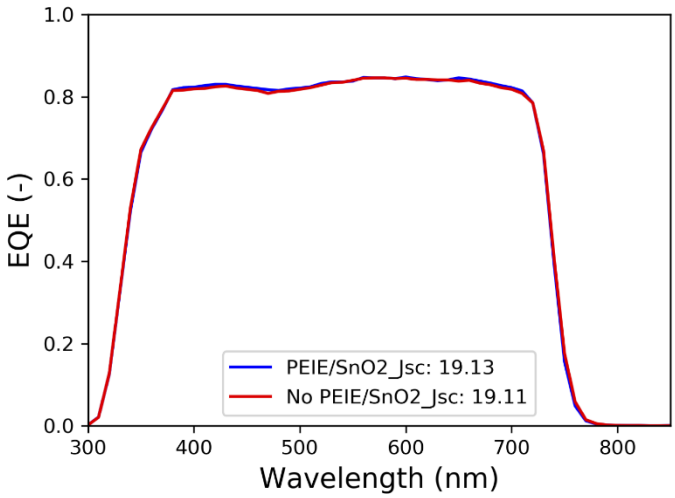

Figure S12: EQE of champion cells with and without PEIE showing little difference and good agreement with measured J_{SC} values.

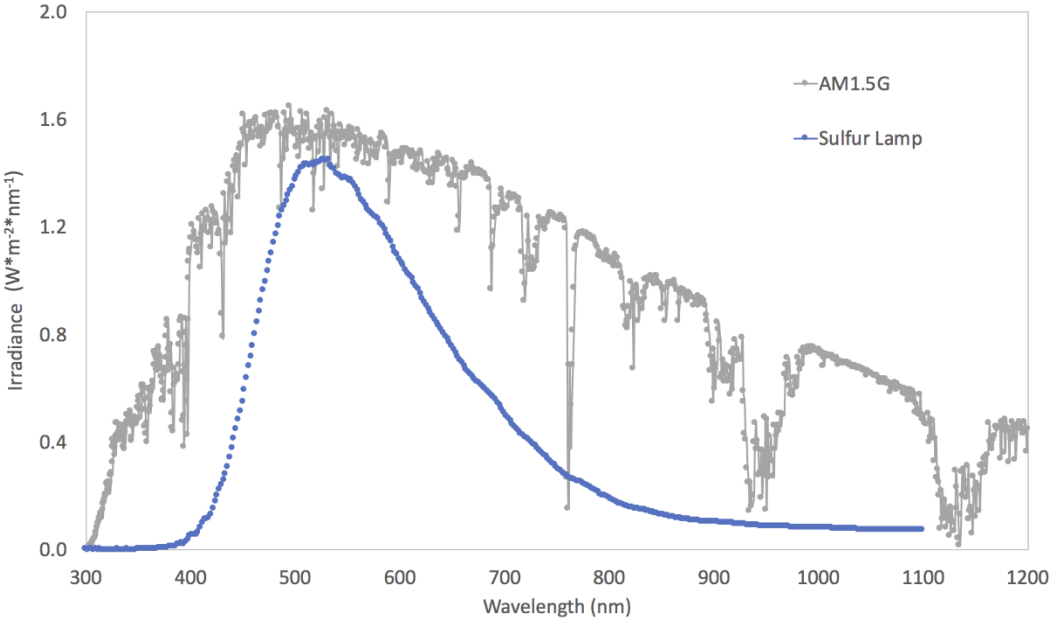

Figure S13: Irradiance spectrum of the sulfur plasma lamp used in this study compared to AM1.5G. Note that this comparison applies to the shape only, as the absolute value of the lamp irradiance is adjusted to match 0.77 sun intensity.

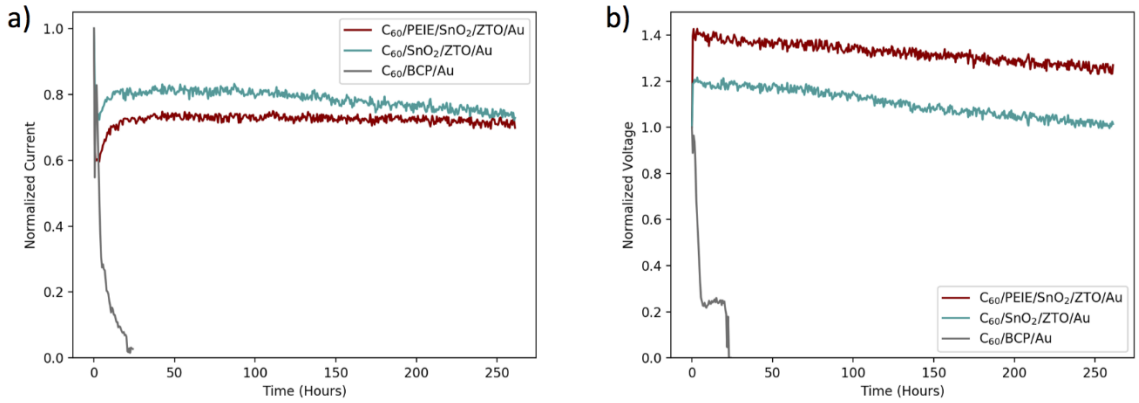

Figure S14: Normalized (a) current and (b) voltage of champion cells with 0.025wt% PEIE/SnO_2, No PEIE/SnO_2, and organic only electron transport layers between the perovskite and the Au top contacts during maximum power tracking in ambient air at 60°C (see Figure 4 for maximum power traces).

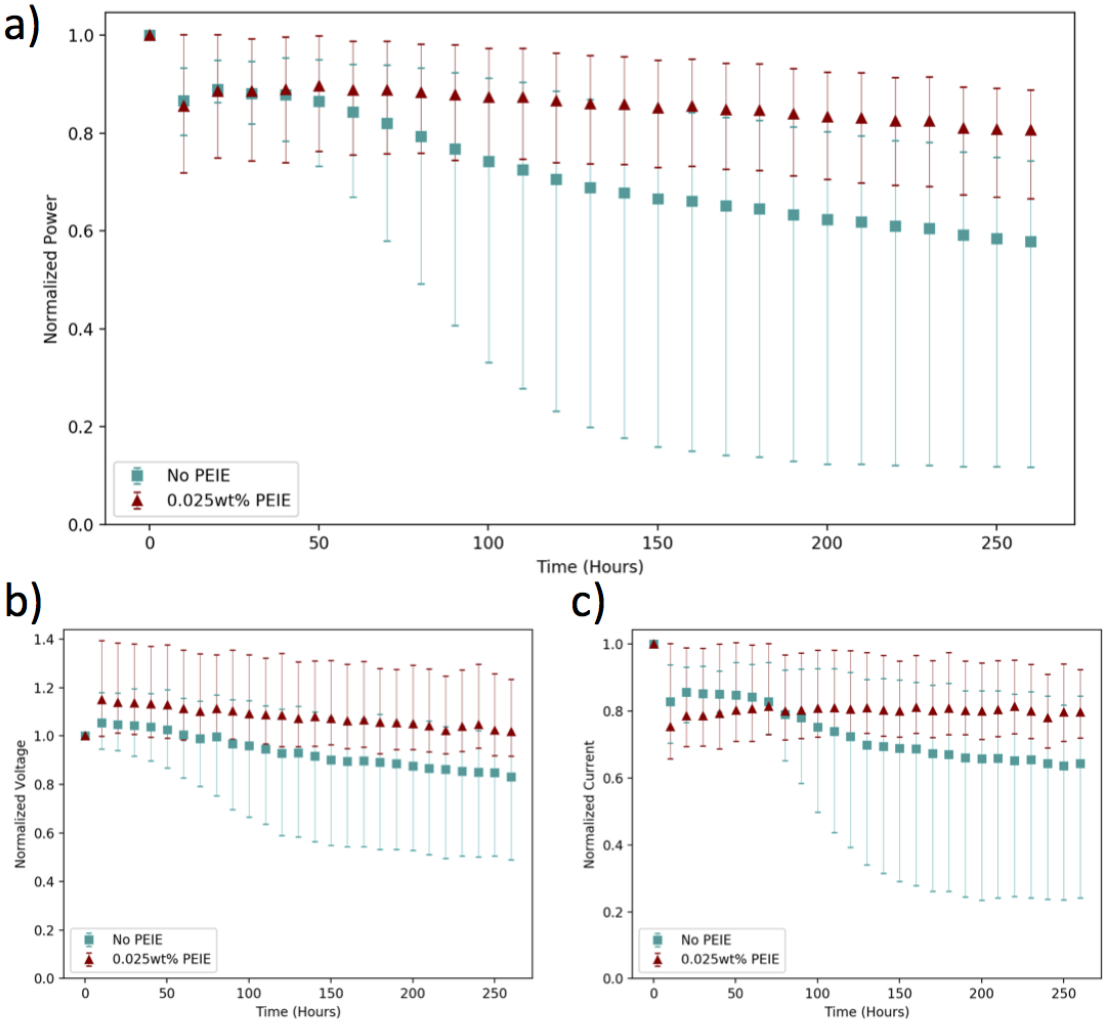

Figure S15: Average values of (a) power, (b) voltage, and (c) current of 8 cells normalized to their initial values with and without PEIE maximum power tracked under 0.77 suns in ambient air at 60ºC. The bars correspond to the maximum and minimum values for each data set, respectively. Data points are only shown every ten hours for clarity.

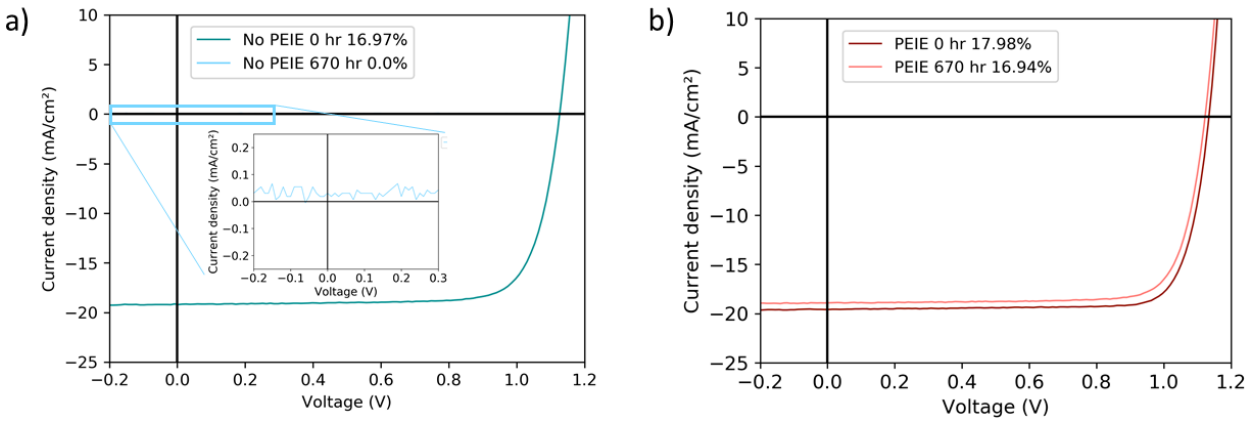

Figure S16: JV before and after hotplate stability testing of cells with and without a PEIE nucleation layer (see Figure 4). (a) Representative JV curve of a solar cell *without* a PEIE nucleation layer showing a total loss in performance after 670 hours at 85°C in the dark in N_2. The cell becomes disconnected because of severe degradation of the top Ag contacts due to metal-halide reactions. (b) Representative JV curve of a solar cell *with* a PEIE nucleation layer before and after 670 hours of hotplate aging. The cell performs very well even after aging.

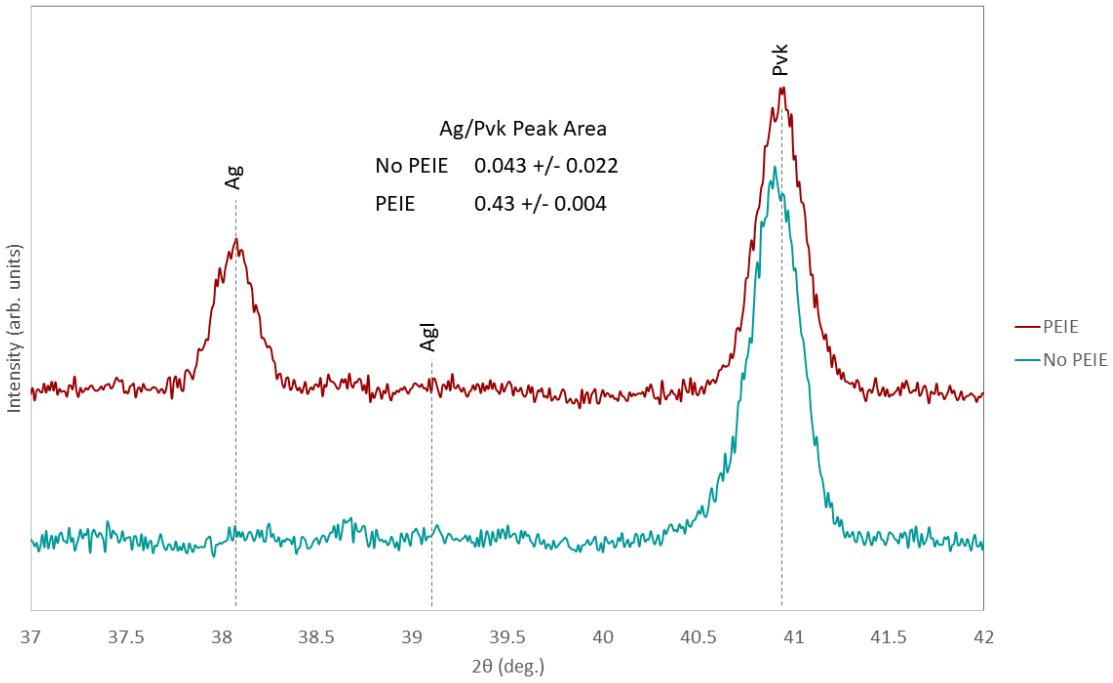

Figure S17: XRD of cells with and without PEIE after hotplate stability testing. The cell with PEIE still has a strong Ag signal, because the improved SnO_2 barrier layer prevented metal-halide reactions. The cell without PEIE has almost no remaining Ag signal. Also shown is the average Ag/perovskite peak area ratio and standard deviation for three different XRD measurements of each type of cell. The cell with PEIE has an order of magnitude improvement in blocking metal-halide reactions as quantified by the Ag/perovskite peak ratio.